Comparison of Ce/Co and Ce/FeNi coatings for interconnects in solid oxide electrolysis

International Journal of Hydrogen Energy 203 (2026) 152996

Contents lists available at ScienceDirect

International Journal of Hydrogen Energy

journal homepage: www.elsevier.com/locate/he

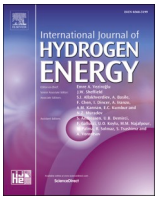

Comparison of Ce/Co and Ce/FeNi coatings for interconnects in solid oxide electrolysis

Mareddy Jayanth Reddy [a], Claudia Goebel [b], Anabelle Valot [c], Ragnar Kiebach [b], Jan-Erik Svensson [a], Henrik Lund Frandsen [b], Jan Froitzheim [a,*]

[a] Chalmers University of Technology, Department of Chemistry and Chemical Engineering, Kemivägen 10, 41296, Gothenburg, Sweden
[b] Department of Energy Conversion and Storage, Technical University of Denmark, Fysikvej Building 310, 2800, Kongens, Lyngby, Denmark
[c] ESIREM - 9, Avenue Alain Savary – BP 47870, 21078 DIJON CEDEX, France

ARTICLE INFO

Keywords:
MCO coating
FeNi coatings
AISI 441
Electrolyser
Interconnect
Oxidation

ABSTRACT

Manganese Cobalt oxide (MCO) coatings have been extensively studied for interconnect applications in solid oxide fuel cells (SOFC). Nevertheless, Co is a critical raw material and efforts are taken to replace it. Ce/FeNi coatings are proposed as an alternative and compared to Ce/Co on AISI 441. Chromium evaporation behaviour, oxidation kinetics, interfacial fracture energy, and area-specific resistance (ASR) of the coating and steels were investigated for up to 3,850 h at 850 °C. Ce/FeNi coatings were not found to be as effective as Ce/Co coatings in preventing chromium evaporation. Nevertheless, Ce/FeNi coated steels showed 50 % lower parabolic rate constant and ASR than Ce/Co coated steel. Additionally, the fracture energy of the adherence of the Ce/FeNi coating to the steel was measured at 750 and 850 °C. The Ce/FeNi coating adherence to the steel greatly outperformed the Ce/Co coating adherence. Furthermore, while the fracture energy of the Ce/Co coating decreases with exposure time, it increases over time for the Ce/FeNi coating.

1. Introduction

Solid oxide cells (SOC) are high-temperature electrochemical devices, which can be operated in either fuel cell mode as solid oxide fuel cell (SOFC) or electrolyser mode as solid oxide electrolyser cell (SOEC). SOFC are highly efficient in converting chemical energy stored in the fuel to electricity [1]. Similarly, high-temperature electrolysis (HTE) with solid oxide electrolysis cells is very effective in producing hydrogen from steam, with efficiencies reported over 93 % HHV [2] (when supplied with waste heat). SOFC and SOEC are being demonstrated globally in numerous projects as part of a push for decentralised energy [3] and hydrogen economy for a low-carbon society [4].

The interconnect is a vital component within the SOC stack, electrically connecting individual cells while separating the fuel and air. The reduction in the working temperature of SOC to the range of 600–850 °C enables the use of metallic interconnects. Among all Cr_2O_3-forming alloys, ferritic stainless steels (FSS) are the most promising candidates owing to their thermal expansion coefficient (TEC) compatibility with other SOC components, electronic conductivity, formability and low manufacturing cost. However, chromia scale growth and chromium evaporation are significant issues when using FSS interconnects. The chromia scale growth increases resistance across the interconnect. Additionally, Cr_2O_3 also reacts with O_2 and H_2O to form volatile $CrO_2(OH)_2$. $CrO_2(OH)_2$ is deposited at the triple-phase boundaries of the air electrode in SOFC, blocking the oxygen reduction reaction, this process being known as chromium poisoning [5]. The overall SOFC reaction is exothermic and large amounts of air with ambient humidity are needed to cool the system. In contrast, this is not needed in SOEC, only a sweep gas might be introduced for safety. Hence, the oxygen side can be very dry, provided no leakage occurs. Consequently, chromium evaporation is not a foremost concern in SOEC. Despite low chromium evaporation in the SOEC atmosphere, it was reported that the chromium contamination of the oxygen electrodes is a significant degradation in the SOEC stacks [6]. The chromium contamination of the oxygen electrodes may be due to solid-state diffusion [7] rather than chromium evaporation. Nevertheless, the chromia scale growth and chromium evaporation lead to Cr depletion in the steel, which may result in the breakdown of the protective oxide over time. Hence, surface modification, achieved through protective coatings is commonly suggested for SOEC interconnects [8,9].

* Corresponding author.
E-mail address: jan.froitzheim@chalmers.se (J. Froitzheim).

https://doi.org/10.1016/j.ijhydene.2025.152996
Received 4 June 2025; Received in revised form 26 July 2025; Accepted 9 December 2025
Available online 22 December 2025

The most studied coating material is MCO (Manganese Cobalt Oxide $(Mn,Co)_3O_4$). MCO-based coatings have been applied using various techniques such as physical vapour deposition [10–12], sol-gel dip--coating [13,14], electrophoretic deposition [15–18], electroplating [19,20], screen printing [21,22], spray pyrolysis [23,24], inkjet printing [25,26], thermal co-evaporation [27,28] and atmospheric plasma spraying [29–31]. The $(Mn,Co)_3O_4$ spinel is very effective in reducing chromium evaporation [8,32–35]. Reactive element (RE) coatings combined with MCO coatings can improve the oxidation resistance of the steel. Several authors [36,37] have shown that adding reactive elements to MCO coatings has a beneficial effect, significantly reducing chromia scale growth. Reactive elements such as Y, La, Ce, Zr, and Hf are known to greatly reduce oxidation rate and improve scale adhesion of Cr_2O_3 and Al_2O_3 forming alloys. The exact mechanism(s) behind this effect are still debated but it is commonly suggested that these additions impede cation transport through the oxide scale. For a more detailed discussion the reader is referred to Refs. [38–40]. MCO coatings can be produced by depositing metallic Co using the physical vapour deposition (PVD) technique in a large-scale roll-to-roll coating process. Metallic Co is converted into MCO. First, Co is oxidized to Co_3O_4 which during stack operation is enriched by Mn from the steel substrate to form $(Mn,Co)_3O_4$. MCO-based coatings have been shown to be highly effective and stable for over 35,000 h [41,42]. Despite the advantages, cobalt compounds can be toxic and harmful to the environment [43]. Moreover, cobalt is defined by the EU as a critical raw material [44] and avoiding Co would provide a significant advantage in terms of cost and material handling.

Ni-based coatings applied using electrodeposition have been reported in the literature [45–48]. The main issue with Ni-based coatings is the transformation of the surface beneath the coating into austenite [45,45,46,48]. Austenite possesses a face-centred cubic (FCC) structure, and its TEC differs from FSS and SOC components [49]. The differences in the TEC can lead to loss of contact with the oxygen electrode. Additionally, the diffusion rate of Cr in the FCC structure is considerably lower than that in the body-centred cubic (BCC) structure [50,51], which can lead to premature breakaway corrosion [47,48]. Due to the potential impact of austenite formation on the durability and longevity of the FSS, Ni-based coatings are not commonly used as protective coatings for interconnects.

Nevertheless, Ni foam/mesh is commonly used on the fuel side as contact between electrode and interconnect. *Piccardo* et al. [52] have studied a metallic interconnect extracted from an SOFC stack after 40,000 h of operation and found Ni diffusion into the interconnect from the fuel side. Ni diffusion was not observed throughout the interconnect but at the contact zones between the Ni foam and the interconnect. This likely happened at the points where the Ni mesh is spot-welded to the interconnect. Although no failure was detected, the authors noted that the presence of an austenitic matrix that could potentially lead to failure after operating for more extended periods, over 40,000 h [52].

Previous studies [53] have demonstrated that austenitic materials, such as alloy 800H, form FeNi-rich oxides on the chromia scale upon oxidation, leading to minimal Cr evaporation. A similar effect can be achieved by applying a $(Fe,Ni)_3O_4$ spinel coating onto a ferritic stainless steel. The TEC of $NiFe_2O_4$ spinel (10.8×10^{-6} K^{-1}) is close to that of the ferritic stainless steels (11×10^{-6} K^{-1}) [54]. The conductivity of $NiFe_2O_4$ spinel (0.26 S cm^{-1}) is significantly lower than the $MnCo_2O_4$ (60 S cm^{-1}) at 800 °C [54]. Nevertheless, the conductivity of the $NiFe_2O_4$ spinel is much higher than the Cr_2O_3 scale (0.001–0.05 S cm^{-1}) [55,56]. *Goebel* et al. [10] and *Reddy* et al. [34] have shown that the conductivity and thickness of the coating do not influence the area-specific resistance (ASR) as the Cr_2O_3 scale dominates the ASR of interconnects. The above attributes make FeNi oxide (FNO) coatings potentially suitable as protective coatings for interconnects. Thus, FNO based coatings [12,57–61] have been studied for the interconnect application.

None of the studies mentioned above has quantitatively determined the effectiveness of these coatings in mitigating chromium evaporation. The chromium evaporation behaviour of most FNO-based coatings was discussed by examining the diffusion of Cr into the spinel. Additionally, very few studies [62] have investigated Ni–Fe based coatings under controlled humidified air flow. Furthermore, none of the above studies have compared FNO-based coatings and MCO coatings. Since the FNO-based coatings appear interesting as a coating for the interconnect in SOFC/SOEC, it is meaningful to study the chromium evaporation behaviour and compare the coating to the state-of-the-art MCO coating. Moreover, also the fracture toughness at the interface of glass sealing, coating and the interconnect is essential to have a robust stack that can withstand thermal cycles. Thus, it is important to understand the interfacial fracture energy at these interfaces for both coating options.

In the present study, the state-of-the-art Ce/Co coating that upon oxidation and Mn diffusion of the steel forms MCO and an Ce/FeNi coating that similarly forms FNO are evaluated and compared with respect to their corrosion behaviour. For this the metallic coating is deposited on AISI 441 using physical vapour deposition; oxidation of the coating in air and at high temperatures then leads to the formation of the desired spinels. Following properties of the coatings were analysed: chromium evaporation behaviour, oxidation kinetics, area-specific resistance and fracture energy for up to 3850 h at 850 °C in air. For completeness, fracture energy measurements were also carried out at 750 °C, facilitating comparison with literature data.

2. Experimental

2.1. Materials

FSS AISI 441, with a composition presented in Table 1, was used as a substrate for the various coatings in the present study. The coatings were applied by Alleima (Sandviken, Sweden) using a proprietary PVD technique. The coatings comprised of a double layer coating of 10 nm Ce (closest to substrate) and 600 nm Co (Ce/Co) and a 10 nm Ce layer and 600 nm FeNi (co,-deposited, 1:1) (Ce/FeNi), respectively. Ce/Co in the as-coated state has been characterised previously [36]. The thickness of the FSS was 0.3 mm for most of the conducted experiments with the exception of the fracture energy measurements, where 0.5 mm thick FSS was used. For chromium evaporation and oxidation experiments, the coatings were deposited on pre-cut steel sheets with a coupon size of 17 × 15 mm^2. On the pre-cut steels, the coupons were attached to the steel frame with two 1-mm joints, resulting in a coating coverage of 99.8 % [33]. For ASR and fracture energy measurements, samples measuring 30 mm × 20 mm were used. The coupons were ultrasonically cleaned in acetone and ethanol for 20 min each to remove any contaminants on the surface.

2.2. Exposures and characterisation

Ce/FeNi-coatings were compared to Ce/Co coatings and uncoated samples. Different exposure conditions were chosen for different measurement techniques. An overview of these is given in Table 2. Details on how these exposures were conducted are given below.

For the oxidation kinetics and Cr evaporation measurements the atmosphere was either dry or humidified air. Pre-dried pressurized air used in the present study has a dew point of −19 °C, (0.1 % H_2O in the air). Humidified air is defined as Air +3 % H_2O in the present study and was achieved by flowing the dry air through a heated water bath (set to ~28 °C) that was further connected to a condenser maintained at a temperature of 24.4 °C to achieve 3 % absolute humidity. The exposures

Table 1
Chemical composition of the selected alloy in weight %.

Alloy	Fe	Cr	C	Mn	Si	Ti	Nb
AISI 441 (1.4509)	Bal	17.56	0.014	0.35	0.59	0.17	0.39

Table 2
Experimental matrix of the present work. Exposure temperature was 850 °C for all experiments.

Material	Furnace	Exposure length	Atmosphere	Analysis
Uncoated 441	Tube furnace	500 h	Dry air Humidified air	Cr evaporation
Ce/Co coated 441	Tube furnace	1,000 h	Humidified air Dry air	Cr evaporation Oxidation kinetics + SEM
	Box furnace	3,850 h	Stagnant laboratory air	ASR + SEM
Ce/FeNi coated 441	Tube furnace	1,000 h	Humidified air Dry air	Cr evaporation Oxidation kinetics + SEM
	Box furnace	3,850 h	Stagnant laboratory air	ASR + SEM
	Box furnace	≤3,000 h		Fracture energy[a] + SEM[a]

[a] These experiments were also carried out at 750 °C.

in dry air and air +3 %H_2O were performed with a continuous flow set at 6,000 sml min^{-1}. A porous SiC flow restrictor was positioned in front of the samples to ensure a uniform flow and to minimise convection. The coupons in the tube furnace were placed in an alumina holder along the direction of the airflow.

Oxidation kinetics: Oxidation kinetics of the coated and the uncoated steels were gravimetrically analysed before and after exposure at 850 °C for 1000 h. The cleaned coupons were weighed using a Mettler Toledo XP7 scale before the exposure. The coupons were removed periodically from the furnace, cooled to room temperature, and the mass gain was recorded before the samples were placed back in the furnace. At least six coupons were used for each oxidation experiment.

Chromium evaporation: Three coupons of each material were used for the chromium evaporation experiments. In-situ chromium evaporation was measured using the denuder technique devised by *Froitzheim* et al. [63]. The reactor's gas stream containing the vapourised chromium species was passed through a denuder tube coated with Na_2CO_3. The vapourised chromium species reacted with the Na_2CO_3 according to Equation (1).

$$Na_2CO_3(s) + CrO_2(OH)_2(g) \rightarrow Na_2CrO_4(s) + CO_2(g) \quad (1)$$

The denuder tubes were replaced periodically without interrupting the exposure. The removed denuder tubes were leached with water, and the solutions were analysed in a Thermo Scientific Evolution 60S spectrometer to determine the time-resolved chromium evaporation of the exposed coupons. The chromium evaporation of the uncoated coupons was measured for 500 h at 850 °C, while the coated coupons were measured for 1,000 h at 850 °C.

Microstructural analysis: The cross-sections of the uncoated, Ce/Co coated and Ce/NiFe coated steels exposed for up to 1,000 h were prepared using a Leica TIC3X™ by broad ion beam (BIB) milling. The microstructure and chemical composition were characterised using the JEOL JSM-7800F Prime SEM equipped with an Oxford Instruments energy-dispersive x-ray spectrometer (EDX). After ASR measurements and fracture energy experiments further microstructural characterisation was carried out by SEM/EDX using a Zeiss EVO microscope MA 10 equipped with an Oxford Instruments X-MAX EDX detector.

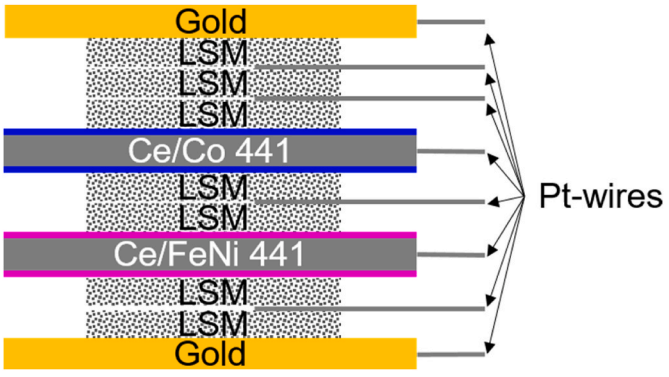

Fig. 1. Schematic drawing of the ASR stack. The Pt wires attached to the steel samples were welded on top of the coated AISI 441.

Area-specific resistance: The area-specific resistance (ASR) of Ce/Co coated and Ce/FeNi coated AISI 441 was measured in-situ by using an experimental setup that has been previously described in detail in Refs. [64,65]. Semi-sintered $La_{1-x}Sr_xMnO_3$ (LSM) plates (2 × 2 cm) were used as current collectors and allowed for simultaneous measurements of multiple samples. The final result of the assembled stack is shown in Fig. 1. Rectangular coupons with a size of 2 × 4 cm were used for the ASR tests.

The ASR measurements were carried out at 850 °C, in stagnant laboratory air, and under a load of 7 kg. A conditioning profile was run during the heat-up period to improve the contact between the separate layers. First, the ASR stack was heated to 600 °C with 15 °C h^{-1}. After 1 h at 600 °C, the temperature was increased further to 800 °C with 60 °C h^{-1}. This temperature was again held for 1 h, after which the temperature was increased to the final exposure temperature of 850 °C. Once the temperature reached 600 °C, a current of 2 A was applied, which resulted in a current density of 0.5 A cm^2. After 3,190 h of isothermal exposure at 850 °C, 50 thermal cycles were conducted. For these, the stack was cycled between 850 °C and 200 °C with a 120 °C h^{-1} heating and cooling ramp and a 2 h dwell time at 850 °C. After the thermal cycles, the stack was cooled to room temperature, embedded in epoxy, and polished to 1 μm diamond suspension. Subsequently SEM/EDX analysis was performed.

2.2.1. Fracture energy

The fracture energy of Ce/FeNi coated AISI 441 was investigated after 300 and 3000 h of exposure at 750 °C and 850 °C.

For this 0.5 mm thick Ce/FeNi 441 sheets were laser cut into 3 mm × 29 mm short bars and 3 mm × 60 mm long bars. Subsequently, the bars were ultrasonically cleaned in ethanol and acetone and then exposed at 750 °C or 850 °C in a box furnace for 300 h or 3,000 h in stagnant laboratory air. After exposure a Ba-free glass-ceramic (46.4 % SiO_2, 13 % MgO, 14.3 % CaO, 9.3 % Na_2O, 8.3 % Al_2O_3, 2.9 % ZrO_2, and 5.8 % B_2O_3) was screen-printed onto the exposed short-bars. For further information on the synthesis and specifications of this glass and the screen printing process, the reader is referred to Refs. [66,67]. The short bars and long bars were assembled in a sandwich-like structure, as shown in Fig. 2a. Subsequently, conditioning of the glass deposited via screen-printing was performed. For this, a load of 16.7 N cm^{-2} was applied to the samples and the following heating profile was applied. First the samples were heated up to 600 °C using a 15 °C h^{-1} heating ramp and held at that temperature for 1 h to allow for the evaporation of binders and solvents. Afterwards, the samples were heated further to 800 °C at 60 °C h^{-1} and another 1 h hold was applied. Finally cooling to room temperature was carried out at 60 °C h^{-1}.

Subsequently, the fracture energy of Ce/FeNi coated AISI 441 was investigated using a four-point bending setup based on previous work by *Charalambides* et al. [68] and *Hofinger* et al. [69] and described in detail

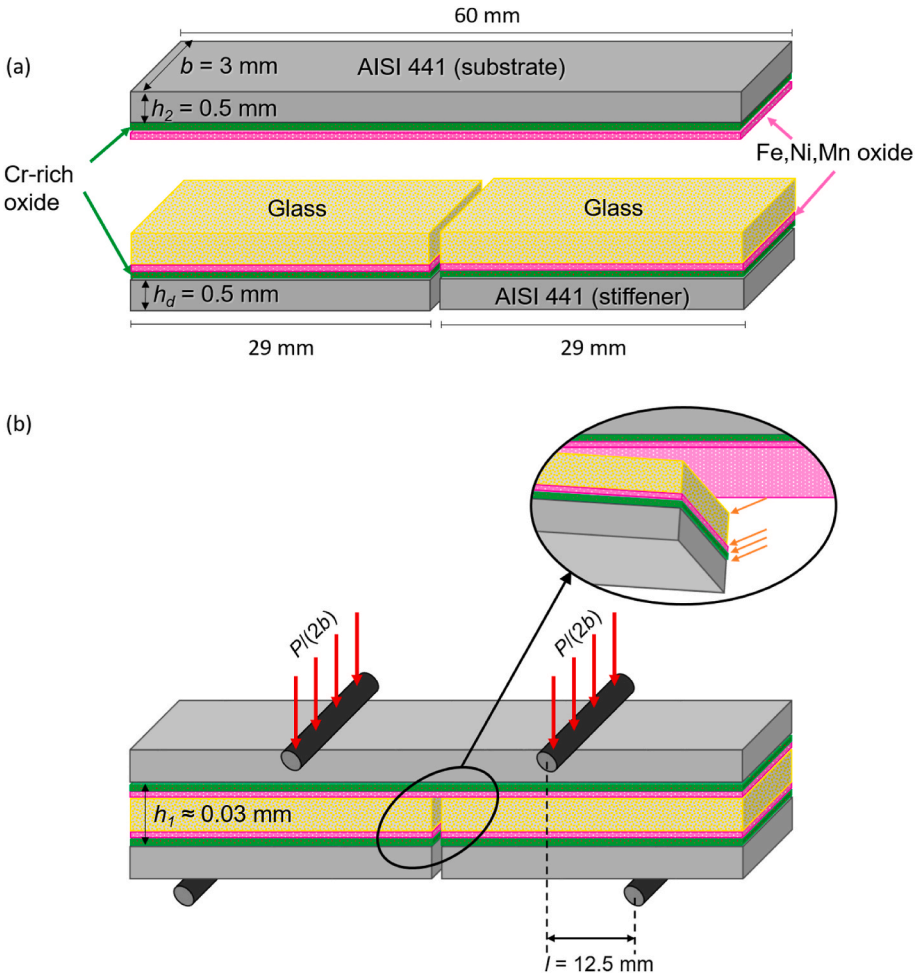

Fig. 2. Schematic drawing of the sample configuration (a) and the 4-point bending test setup (b) based on [69].

in Refs. [70,71]. A schematic of the testing setup is shown in Fig. 2. Using this setup, five samples were tested at room temperature for each test condition to measure the fracture energy along the interface between two layers. Bending of the sandwiched sample was achieved by moving the top-pins towards the bottom-pins with a displacement rate of 0.01 mm s^{-1}, while both displacement and load were recorded. From this data the bending moment M_b was calculated according to Equation (2) using the maximum load P at crack propagation, the distance between outer and inner pins, l, and the width of the sample, b (see Fig. 2).

$$M_b = \frac{Pl}{2b} \tag{2}$$

The fracture energy, G_c, was then determined according to the method established by *Charalambides* et al. [68] and refined by *Hofinger* et al. [69] (see Equation (3)).

$$G_c = \frac{M_b^2(1-\nu_2^2)}{2E_2}\left(\frac{1}{I_2}-\frac{1}{I_c}\right) \tag{3}$$

With the poisson ratio, ν, the Young's modulus, E, and the second moment of area, I, and where the index *2* refers to the long metal bar, also called substrate (see Fig. 2), and the index c refers to a combined value. The second moment of area are defined according to Equations (4) and (5).

$$I_2 = \frac{h_2^3}{12} \tag{4}$$

$$I_c = \frac{h_2^3}{3} + \kappa\frac{h_1^3}{3} + \mu\left(\frac{h_d^3}{3} + h_d^2 h_1 + h_1^2 h_d\right) - \frac{\left[h_2^2 - \kappa h_1^2 - \mu\left(h_d^2 + 2h_1 h_d\right)\right]^2}{4(h_2 + \kappa h_1 + \mu h_d)} \tag{5}$$

Where h describes the layer thickness and index d refers to the short metal bars, also called stiffener. The index *1* refers to the layer between the two metal bars, which in the present case comprises the different oxide scales and the glass (see Fig. 2) and κ and μ are defined according to Equations (6) and (7), respectively.

$$\kappa = \frac{E_1(1-\nu_2^2)}{E_2(1-\nu_1^2)} \tag{6}$$

$$\mu = \frac{E_d(1-\nu_2^2)}{E_2(1-\nu_d^2)} \tag{7}$$

For the present work ν_2 and ν_d were assumed to be 0.3, which is a typical poisson's ratio for stainless steels [72] and the Young modulus for AISI 441 was taken from the respective datasheet ($E_2 = E_d = 220$ GPa [73]). No precise values were available for the poisson's ratio or for the Young modulus of the glass, however as the calculation of G_c is very robust to variations of both values, ν_1 was set to 0.2 and E_1 was set to 76 GPa [70,74].

To understand the fracture mechanisms top-view and cross-sectional SEM was carried out on the tested specimens (the top-view images were mirrored for easier comparison). For the top-view SEM, the tested sandwiched sample was pulled fully apart by hand after mechanical testing. For the cross-sectional SEM, the samples were embedded in Epoxy and polished to 1 μm diamond suspension. The subsequent

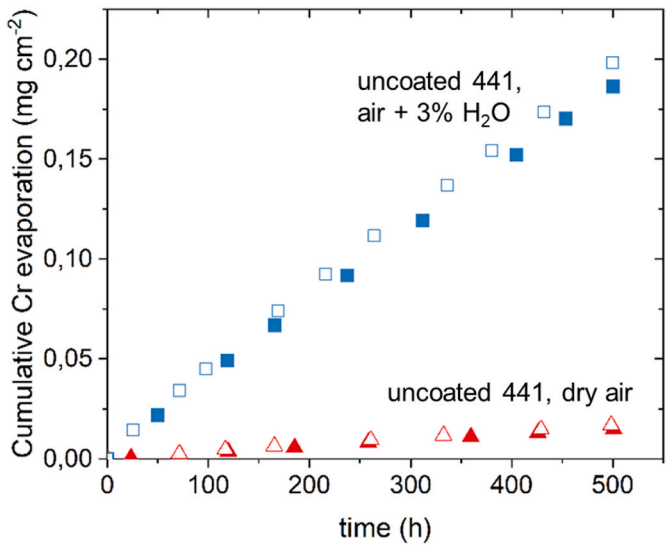

Fig. 3. (a) Cumulative chromium evaporation of the uncoated 441 in dry air and humidified air (3 % H_2O) at 850 °C for 500 h. Open and closed symbols represent individual experiments.

analysis focused on the area nearest to the notch, corresponding to the region fractured during the four-point bend test.

3. Results and discussion

Fig. 3 shows the chromium evaporation of the uncoated AISI 441 exposed to air +3 %H_2O and dry air for 500 h at 850 °C. The cumulative chromium evaporation of AISI 441 in humidified air is one order of magnitude higher than in dry air.

$CrO_2(OH)_2$ and CrO_3 are reported to be the most abundant vapour species in high oxygen partial pressure environments with and without humidity, respectively [75,76]. The involved chemical reactions are presented in Equations (8) and (9).

$$\frac{1}{2}Cr_2O_3 + H_2O + \frac{3}{4}O_2 \rightarrow CrO_2(OH)_2(g) \quad (8)$$

$$\frac{1}{2}Cr_2O_3 + \frac{3}{4}O_2 \rightarrow CrO_3 \quad (9)$$

Based on thermodynamic data for CrO_3(g) [77] and $CrO_2(OH)_2$(g) [77] at 850 °C, it is found that $CrO_2(OH)_2$ is the most dominant species when the water vapour content is over 0.1 % (absolute humidity). Thus, when exposed to air +3 %H_2O, $CrO_2(OH)_2$ is the dominant Cr species with a partial pressure of 1.35 $\times 10^{-7}$ bar at equilibrium. However, the equilibrium partial pressure of $CrO_2(OH)_2$ decreases significantly when the water vapour content is reduced. Hence, in 'dry air' (with an absolute humidity of 0.1 %), both $CrO_2(OH)_2$ and CrO_3 have similar equilibrium partial pressure of 1 $\times$ 10^{-8} bar. However, it should be noted that the experimental conditions are not in equilibrium, and the uncoated AISI 441 surface is covered with $(Cr,Mn)_3O_4$ spinel.

The chromium evaporation of uncoated AISI 441 in a dry atmosphere after 168 h is 5.8 x 10^{-3} mg cm^{-2}. *Alnegren* et al. [78] have reported that the chromium evaporation of a similar material, Crofer 22H, in Ar-25 % O_2 is 1 x 10^{-3} mg cm^{-2} after 168 h. The difference in chromium evaporation between both studies is attributed to the higher flow rate (6L/min compared to 1L/min) in the present study and possibly a difference in humidity. The chromium evaporation is expected to increase when the partial pressure of O_2 is increased ($\propto pO_2^{0.75}$) according to Equation (3). However, *Alnegren* et al. [78] reported a linear dependence of oxygen partial pressure to chromium evaporation in oxygen at 850 °C. Apart from humidity, chromium evaporation in SOEC depends on factors such as the partial pressure of O_2 and flow rate.

After 500 h, the oxide scale on uncoated 441 exposed to humidified air remained mostly intact and continuous, while the oxide scale of uncoated 441 exposed to dry air had spallen off. Other researchers have reported similar results with extensive chromia scale spallation in the absence of water vapour but much less in the presence of water vapour [79,80]. It has been suggested that the oxide scale grown in the presence of water vapour is more plastic due to the smaller oxide grain size compared to the oxide scale grown in the absence of water vapour [81]. Moreover, coating AISI 441 with 10 nm Ce and further exposing it to a dry atmosphere showed no signs of spallation until 1000 h. This might be due to the increased oxide scale plasticity in the presence of reactive elements [38].

As the rate of chromium evaporation in dry air is much lower than in humidified air, further chromium evaporation measurements of coated AISI 441 were performed in humidified air. Fig. 4 shows the cumulative chromium evaporation and rate of chromium evaporation of Ce/Co-coated and Ce/FeNi-coated 441 in humidified air (3 % H_2O) at 850 °C for 1000 h. The chromium evaporation of both coated steels is lower than the uncoated 441 after 500 h shown in Fig. 3. This indicates that the present coatings act as a barrier to chromium evaporation. Nevertheless, the effectiveness of the coatings varied significantly. Ce/FeNi-coated 441 exhibited a factor of 4, while the Ce/Co-coated 441 exhibited a factor of 100 times lower chromium evaporation than uncoated 441. Based on the chromium evaporation data, it appears that the Ce/FeNi coating is not ideal for SOFC atmospheres as the chromium evaporation is substantially higher than the state-of-the-art Ce/Co coatings. However, as explained previously, Cr evaporation appears to be less of a problem in SOEC. Therefore, despite its inferior Cr blocking capability, Ce/FeNi coating can still be suitable for SOEC.

Fig. 5 shows the oxidation kinetics represented by the mass gains of the Ce/Co and Ce/FeNi coated steels exposed to dry air at 850 °C for 1000 h. Fig. 5a shows the mass gain of the coated steels measured at regular intervals until 1000 h. The mass gain of uncoated 441 is not presented because spallation is observed during the thermal cycles. During the first 30 min, both coated steels show a rapid increase in mass gain. This is due to the oxidation of the metallic coatings from Co to Co_3O_4 [10,82,83] and FeNi to $(Fe,Ni)_3O_4$ [12,58,59]. The subsequent slower mass gain observed is mainly due to the oxidation of Cr to Cr_2O_3 [82]. During this period, both steels showed a continuous increase in mass gain, representing parabolic oxidation kinetics. After 1000 h, a significant difference is observed in the mass gain between Ce/Co-coated 441 and Ce/FeNi-coated 441. The mass gain of Ce/Co coated 441 is 0.89 $\pm$ 0.02 mg $cm^{-2,}$ while Ce/FeNi is 0.62 $\pm$ 0.01 mg cm^{-2}, excluding the oxidation of the metallic coating.

Fig. 5b shows the oxidation kinetics, represented by Δm^2 vs time. The oxidation rate constant (k_p) was calculated from the mass gain data in Fig. 5a for the Ce/Co- and Ce/FeNi-coated 441. For plotting Δm^2 over time, the mass gain due to coating oxidation (the mass gain data after 30 min) is subtracted from subsequent data points. The straight lines indicate Ce/Co- and Ce/FeNi-coated 441 follow parabolic oxidation kinetics. The k_p of the Ce/Co coated 441 is 0.76 $mg^2cm^{-4}h^{-1}$ while Ce/FeNi coated 441 is 0.39 $mg^2cm^{-4}h^{-1}$. The oxidation rate of the Ce/FeNi-coated 441 is a factor of two lower than the Ce/Co-coated 441. This indicates that the growth of the chromia scale is much lower on Ce/FeNi-coated 441 than on Ce/Co-coated 441. It should be noted that the difference in mass gain can not be attributed to the different mass losses due to Cr evaporation as these are negligible due to the dry environment used for oxidation tests.

Fig. 6 shows the BIB milled cross-sectional micrographs and EDX maps of the Ce/Co- and Ce/FeNi-coated steels exposed to dry air at 850 °C for 1000 h. The oxide scale on both coated steels is continuous, with no signs of spallation. Moreover, the oxide scale on the coated steels comprises of a cap layer and a chromia scale beneath it. The chromia scale on the Ce/FeNi-coated 441 is thinner than the chromia scale observed on Ce/Co-coated 441, consistent with the mass gains observed in Fig. 4. Due to its thinner chromia scale, Ce/FeNi-coated 441 is

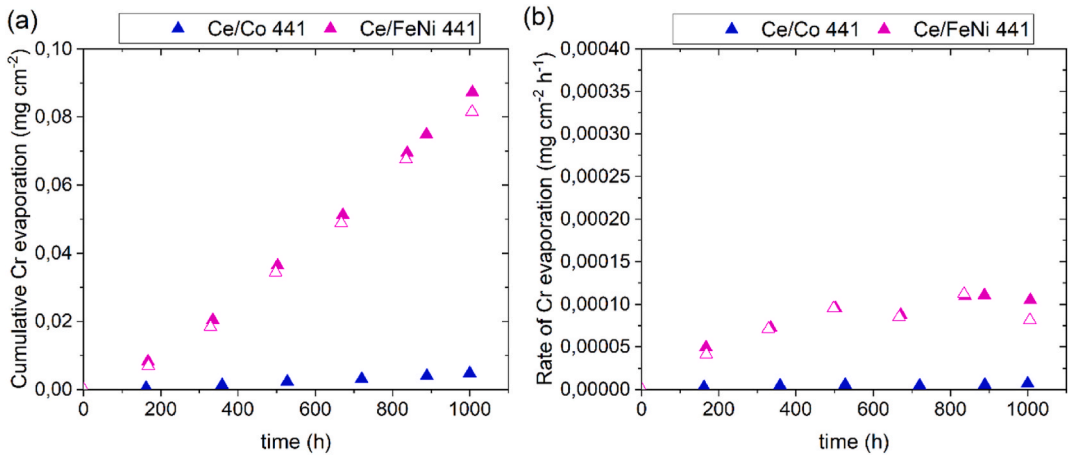

Fig. 4. (a) Cumulative chromium evaporation (b) rate of chromium evaporation of the Ce/Co- and Ce/FeNi-coated 441 in humidified air (3 % H_2O) at 850 °C for 1000 h.

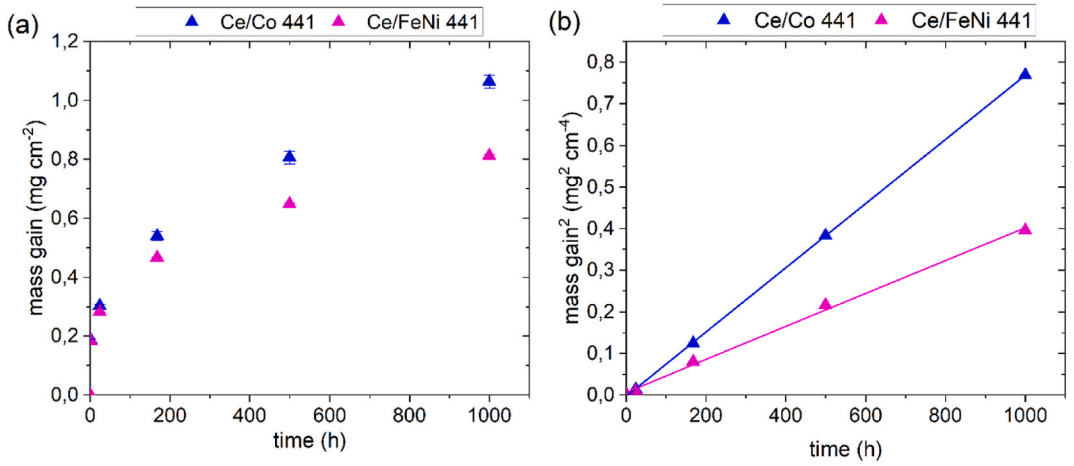

Fig. 5. (a) mass gain (b) mass gain^2 vs time of the Ce/Co- and Ce/FeNi-coated 441 in dry air at 850 °C for 1000 h.

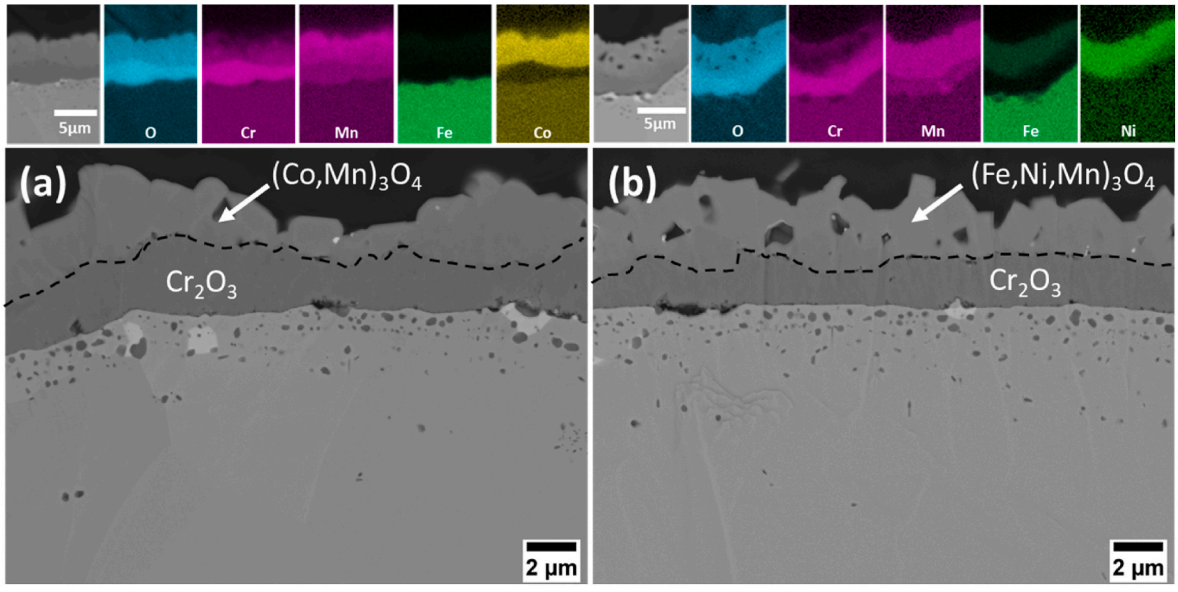

Fig. 6. SEM micrographs and corresponding EDX maps in the cross-section of the (a) Ce/Co- (b) Ce/FeNi-coated AISI 441 exposed to 850 °C for 1000 h in dry air.

expected to have a lower ASR than Ce/Co-coated 441. Despite the presence of Ni in the coating, no austenitisation of the substrate is observed. This is attributed to the fast oxidation of the coatings and intermediate Ce layer between the steel and Ni-containing coating, which acts as a diffusion barrier in the initial stage [83].

The cap layer of Ce/Co-coated 441 is $(Co,Mn)_3O_4$ spinel, which has been thoroughly characterised in previous studies at 850 °C in air + 3 % H_2O [42,82]. It was found that the oxide layer is comprised of inner chromia scale and outer $(Co,Mn)_3O_4$ spinel almost free of Cr [82]. In the present case (dry air), the morphology is the same with an inner chromia scale and outer $(Co,Mn)_3O_4$ spinel. However, up to 10 at% Cr is found in the $(Co,Mn)_3O_4$ spinel after 1000 h. *Magdefrau* et al. [84] have reported the formation of $(Co,Mn)_3O_4$ spinel + Cr reaction layers in MCO coatings exposed to 800 °C in air for 1000 h. Furthermore, *Reddy* et al. [34] reported that such $(Co,Mn)_3O_4$ spinel + Cr reaction layers are observed in MCO-coated steels exposed to high temperatures above 900 °C. Further studies on MCO coatings with varying water vapour content are required to understand this behaviour.

The cap layer on the Ce/FeNi-coated 441 is $(Fe,Ni,Mn)_3O_4$ spinel. The $(Fe,Ni)_3O_4$ spinel formed during the initial 30 min of exposure transformed to $(Fe,Ni,Mn)_3O_4$ spinel owing to the diffusion of Mn from the steel to the coating. Up to 5 at% of Cr is observed in the spinel, mainly at the chromia coating interface. *Geng* et al. [60] reported the formation of $(Ni,Fe,Cr)_3O_4$ spinel due to the Cr diffusion.

The recorded ASR values are shown in Fig. 7. During the isothermal exposure three unplanned thermal cycles occurred after 1,200 h, 1,350 h, and 2,065 h of exposure. The average ASR values after 3,190 h of isothermal exposure, and after thermal cycling and the degradation rates for all examined materials are shown in Table 3. The degradation rates were calculated using a linear regression based on the last 500 h of exposure for the isothermal case and on all 50 thermal cycles for the thermal cycling case.

During the first 1,200 h of isothermal exposure Ce/Co- and Ce/FeNi-coated 441 showed similar ASR values. However, after the first thermal cycle Ce/Co-coated 441 showed an increase in its degradation rate, which was not observed for Ce/NiFe-coated 441. A similar behaviour is

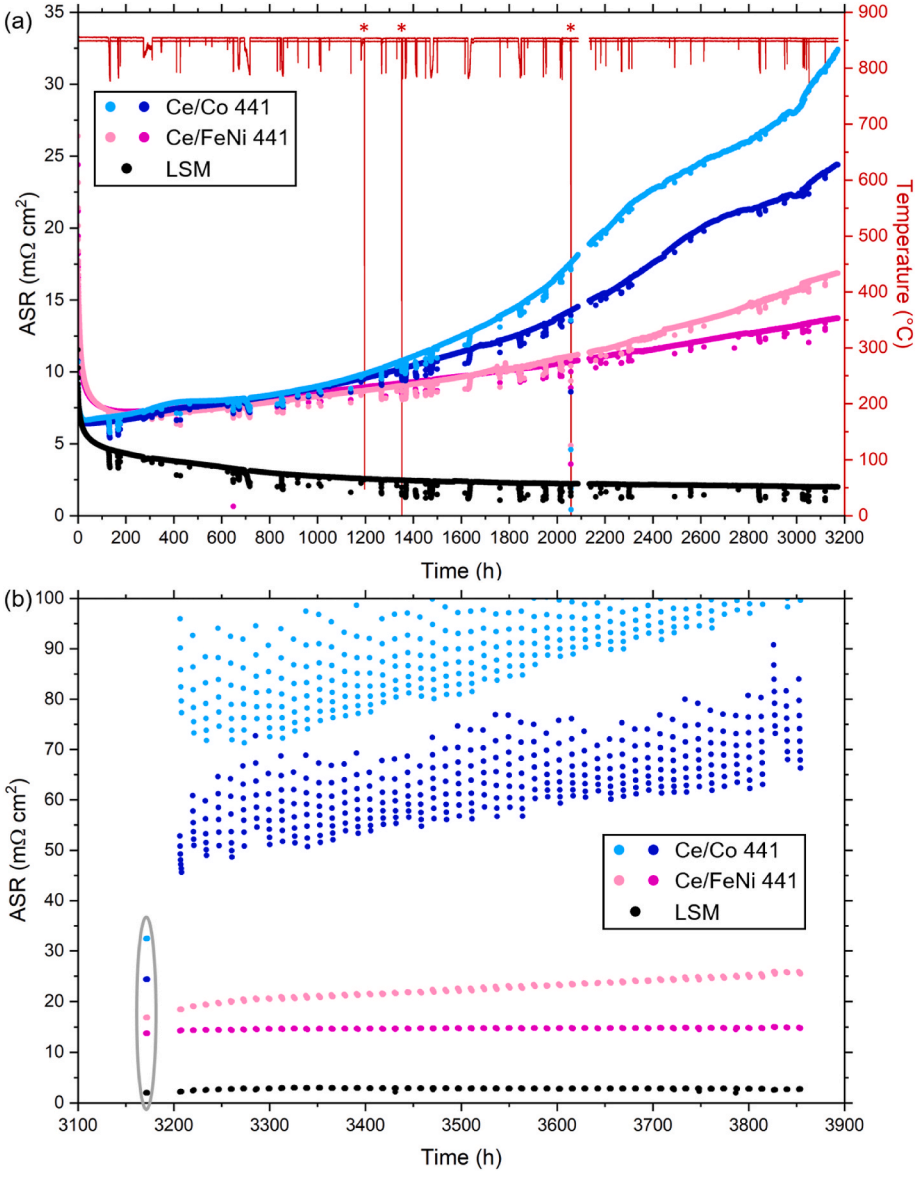

Fig. 7. In-situ ASR measurements conducted on Ce/Co- and Ce/FeNi-coated AISI 441 at 850 °C in laboratory air with (a) isothermal exposure including three unplanned thermal cycles (marked with an asterisk, after 1,200 h, 1,350 h and 2,065 h), and (b) 50 subsequent thermal cycles. During the thermal cycles, the samples were cycled between 850 and 200 °C. For clarity, only the values recorded at 850 °C are shown. The data inside the grey ellipse correspond to the last data points recorded during isothermal exposure, shown in (a).

Table 3
ASR measured at 850 °C during 3,190 h of isothermal aging and 50 subsequent thermal cycles down to 200 °C. Degradation rates were determined using linear regression.

Material	Isothermal aging		Thermal cycling	
	ASR after 3190 h [mΩcm^2]	Degr. Rate[a] [mΩcm^2/1,000 h]	ASR after 50 thermal cycles [mΩcm^2]	Degr. Rate[b] [mΩcm^2/1,000 h]
LSM	2.0	−0.2	2.7	0
Ce/Co-coated 441	28.4 ± 4.1	10.7 ± 4.9	83.0 ± 23.6[c]	37.4 ± 12.3[c]
Ce/FeNi-coated 441	15.3 ± 1.6	4.5 ± 2.5	20.2 ± 5.6	5.1 ± 6.4

[a] Degradation rates were determined over the last 500 h of ASR measurements.
[b] Degradation rates calculated based on the 50 thermal cycles.
[c] These values experienced a relaxation phase, and the ASR value had not yet reached a steady state at the end of each cycle; therefore, the results might be higher than the true values.

seen for each subsequent thermal cycle. After isothermal exposure the average ASR value as well as the degradation rates were approximately double for Ce/Co-coated 441 than for Ce/FeNi-coated 441. Both the average values and the degradation rate for Ce/Co-coated 441 were similar to values reported by *Talic* et al. [85] after isothermal exposure.

The degradation rates and the average values for Ce/FeNi-coated 441 after thermal cycling (see Table 3) are similar to the values after isothermal exposure, considering their margin of error. The Ce/Co-coated 441 showed an interesting behaviour during the thermal cycling. After each thermal cycle, the ASR values spiked and then relaxed over time. It could be hypothesized that the relaxation process is nearly complete after 2 h as the gap between the separate measurement values seems to decrease drastically the end of the 2 h (see Fig. 7). Nevertheless, the relaxation was not yet fully completed after the 2-h hold time at 850 °C, hence the spread in the data in Fig. 7. Additionally, this implies that neither the average values nor the degradation rates for Ce/Co-coated 441 presented in Table 3 are completely reliable. Ce/FeNi-coated 441 did not show this relaxation behaviour and instead the ASR values recorded after each cycle showed minimal difference to the value recorded in the preceding cycle. This observation suggests that the contact between Ce/FeNi-coated 441 and the LSM layer is more robust towards thermal cycling than the contact between the Ce/Co-coated 441 and the LSM. This could in turn also explain, why Ce/Co-coated 441 seemed to degrade after each unplanned thermal cycle during the isothermal exposure, especially, because unplanned thermal cycles often see a drastic temperature drop instead of a well-controlled temperature decrease. *Talic* et al. [85] did not see this relaxation behaviour during the thermal cycling of Ce/Co-coated 441, however, they did observe this behaviour during thermal cycles that occurred during the isothermal exposure, further strengthening the hypothesis that the relaxation process might be nearly complete after the 2 h hold. In general, Ce/FeNi-coated 441 shows lower ASR values compared to Ce/Co-coated 441. Additionally, Ce/FeNi-coated 441 seems more robust towards thermal cycling than Ce/Co-coated 441.

Figs. 8 and 9 show the SEM micrographs and EDX maps, respectively, that were recorded after the ASR measurements. For both materials, Ce/Co- and Ce/FeNi-coated 441, the SEM micrographs showed a detachment of the LSM layer from the coated steel. The detachment occurred during sample preparation, i.e. during dismounting, epoxy embedding and subsequent grinding and polishing of the samples, because otherwise, much higher ASR values would have been measured. The SEM analysis also showed that a two-layered oxide scale had formed for both Ce/Co- (Fig. 8a1) and Ce/FeNi-coated 441 (Fig. 8b1). In combination with the EDX maps and additional EDX point analysis, it was determined that the inner oxide layer consisted of a Cr-rich oxide, and the outer oxide layer was either a Cr,Mn,Co-oxide for Ce/Co-coated 441, or a Cr, Fe,Mn,Ni-oxide for Ce/FeNi-coated 441. In both cases, similar amounts of Cr were detected in the outer oxide scale. At the interface between the Cr-rich oxide and the spinel, both materials showed Cr concentrations of up to 15 at%. This concentration decreased to 7 at% at the oxide/LSM interface. Lower Cr content values were found for the 1,000 h exposed samples described above and shown in Fig. 6. This could be explained not only by the difference in exposure lengths but also due to the stagnant laboratory air that was used for the ~3,800 h exposed samples. It

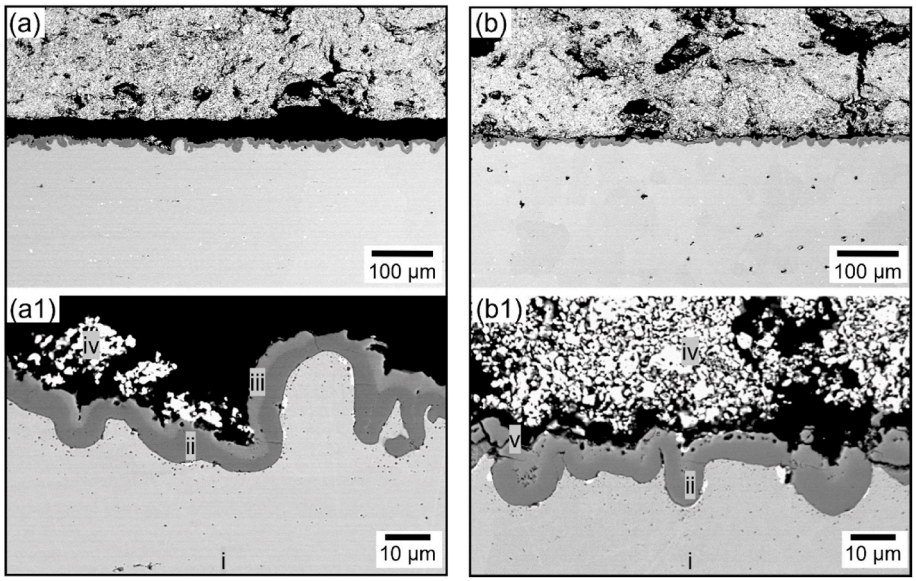

Fig. 8. SEM micrographs of Ce/Co coated 441 (a and a1) and Ce/FeNi coated 441 (b and b1), which were exposed for 3,850 h at 850 °C under current. The phases were identified as follows using EDX: i) 441, ii) a Cr-rich oxide scale, (iii) a Co-rich oxide scale iv) LSM, and v) a Ni,Fe-rich oxide scale (vii).

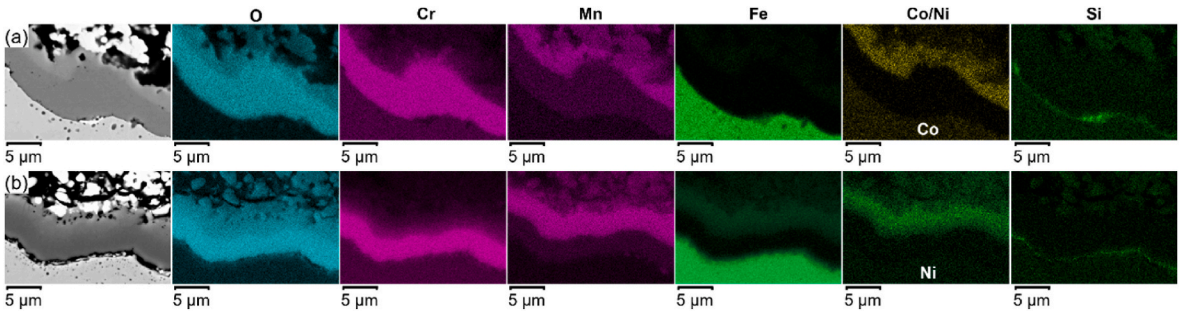

Fig. 9. EDX maps of (a) Ce/Co- (b) Ce/FeNi-coated 441 samples, which were exposed for approx. 3,800 h at 850 °C under current.

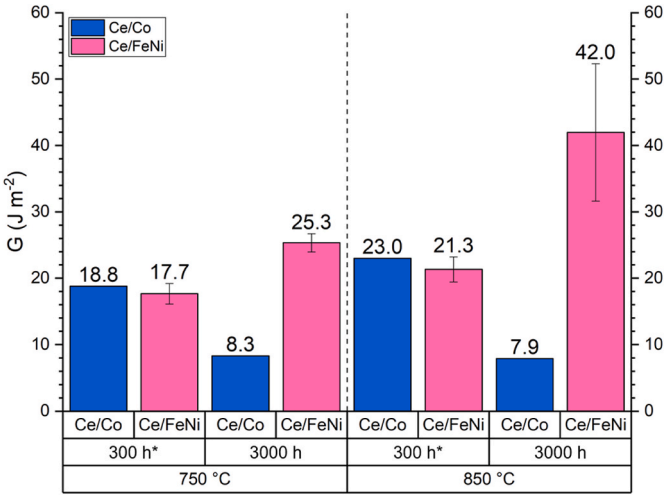

Fig. 10. Fracture energies of coated AISI 441 exposed to stagnant laboratory air at 750 or 850 °C and measured using a 4-point bending test setup. Values for Ce/Co coated AISI 441 were taken from *Farzin* et al. [67]. Multiple samples were measured for each *For the shorter exposure length the Ce/Co coated AISI 441 samples were exposed for 250 h, whereas the Ce/FeNi coated samples were exposed for 300 h.

has been previously shown that samples exposed to stagnant laboratory air retain higher levels of Cr in the outer oxide scale [42].

The Cr-rich oxide scale for Ce/Co-coated 441 was thicker (4.6 ± 1.0 µm) than for Ce/FeNi-coated 441 (3.5 ± 0.9 µm). This aligns with the slower oxidation kinetics observed in the latter case (see Fig. 5) and explains the lower ASR results for Ce/FeNi-coated 441 compared to Ce/Co-coated 441. As previously mentioned, the primary contributor to ASR is assumed to be the Cr-rich scale due to its significantly lower conductivity compared to the spinels used as coatings [10,34]. Consequently, a thinner Cr-rich oxide scale would result in lower ASR values. The lower ASR values cannot be attributed to chromium evaporation as the measurements were recorded in stagnant laboratory air, therefore, Cr evaporation is considered negligible.

A direct comparison of the fracture energies measured by the specific 4-point bending of Ce/FeNi coated 441 and Ce/Co coated 441 can be seen in Fig. 10. The latter values were taken from *Farzin* et al. [67]. For the shorter exposure times, the literature values were recorded after 250 h of exposure in laboratory air, compared to 300 h of exposure in the present study. This time difference is not expected to significantly affect the results. For the short exposure times the fracture energies for Ce/FeNi and Ce/Co coated 441 were similar, approximately 18 J/m^2 at 750 °C and approximately 22 J/m^2 at 850 °C. However, after 3,000 h a clear difference could be seen. For Ce/Co-coated 441 a decrease in fracture toughness was found and the fracture toughness was around 8 J/m^2 after 3,000 h of exposure regardless of the temperature. In contrast, the fracture energy for Ce/FeNi-coated 441 increased with exposure time, reaching an average value of 25 J/m^2 after 3,000 h at 750 °C and 42 J/m^2 after 3,000 h at 850 °C. It should be noted that the data for the Ce/FeNi coated 441 exposed for 3,000 h showed a high fracture energy with a large standard deviation. However, the consistent trend of higher fracture energies after longer exposure times at both 750 and 850 °C indicates that the overall results remain reliable, and that the variation more likely stems from that some areas were not strengthened to the same extent as others over the 3,000 h. Each of the processing steps (screen printing, oxidation, forming of new oxides) will introduce variations across the samples. We speculate that these variations are more noticeable for the stronger oxides, which consequently results in moderately higher standard deviation, nevertheless, a clear strengthening is observed.

To identify the fracture location, SEM micrographs of Ce/FeNi-coated 441 exposed to 750 °C or 850 °C are shown in Fig. 12 or Fig. 11, respectively. The corresponding EDX data for the identified phases are presented in Table S1 and Table S2. For results on Ce/Co-coated 441 the reader is referred to *Farzin* et al. [67]. Those authors concluded, that for Ce/Co-coated 441, the fracture occurs primarily at the steel/oxide interface, regardless of exposure temperature or exposure length.

After 300 h of exposure at 850 °C the SEM top view micrographs show a high surface coverage of the top bar in phase I, which was identified as the glass (see Fig. 11a and Table S1). In some areas a (Cr,Fe,Ni,Mn)-oxide (phase II) was identified and in very few and small areas the underlying steel (phase iii) was detected. The respective bottom bar, shown in Fig. 11b, showed a similar pattern as the top bar (see Fig. 11a), with the glass phase (phase I) covering the majority of the surface. However, the area covered by glass in the top bar is slightly smaller than the area covered by glass in the bottom bar. The two other phases identified in the bottom bar correspond to a Cr-rich oxide (phase IV) and a (Cr,Fe,Ni,Mn)-oxide (phase V). The former is probably situated at the same location where steel (phase III) was detected on the top bar, and the latter is instead located where a (Cr,Fe,Ni,Mn)-oxide (phase II) was also found on the top bar. This suggests that the fracture for these samples occurred primarily in the glass and in some areas in the oxide scale. In very few areas the fracture also occurred along the steel/oxide or the oxide/glass interface. The latter would correspond to the areas where the glass-covered area is larger on the bottom bar than on the top bar. This interpretation suggests that the fracture energy for these samples, 21.3 ± 1.9 J//m^2, corresponds primarily to the fracture energy of the glass.

The SEM micrographs recorded after 3,000 h of exposure at 850 °C show that the surface of the top bar is approximately equally covered by glass (phase I) and a (Cr,Fe,Ni,Mn)-oxide (phase VI) (see Fig. 11c and Table S1). In some small areas a steel signal was also detected (phase VII). The respective bottom bar (see Fig. 11d) showed a similar pattern than the top bar with only two identifiable phases roughly present, the glass (phase I) and a (Cr,Fe,Ni,Mn)-oxide (phase VIII). For this sample no third phase could be identified. The glass covered area for this sample is also smaller in the top bar than the bottom bar. The results suggest that the fracture for this sample occurred to a similar extent in the glass phase

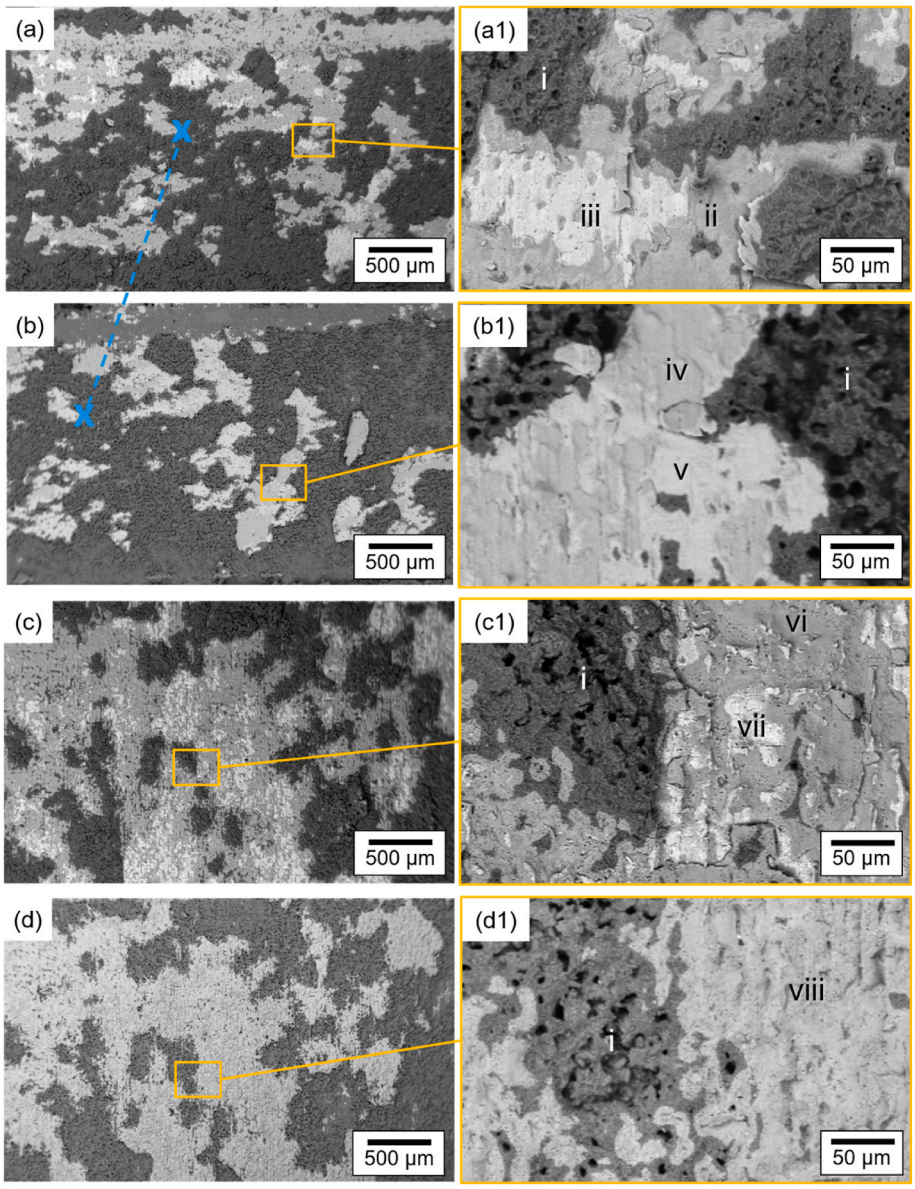

Fig. 11. SEM micrographs of the fracture interface of Ce/FeNi coated AISI 441, which was exposed at 850 °C to stagnant laboratory air for 300 h (a, b) or 3,000 h (c, d). The long top bars are shown in (a) and (c) and the short bottom bars in (b) and (d). The marked 'x' in (a) and (b) indicates a corresponding feature to assist in location correlation. Different phases were identified as follows using EDX: glass (i), oxide-scales (ii, iv, v, vi, viii), and steel (iii, vii). The exact EDX compositions can be found in Table S1.

or in the oxide scale and to a much lesser extent at the steel/oxide interface or the oxide/glass interface. Therefore, the measured fracture energy of 42.0 ± 10.3 J/m^2 corresponds to the average fracture energy of the glass and the oxide scale.

At 750 °C, after 300 h of exposure, the SEM micrographs show a high surface coverage of the top bar in phase I and phase II, which were identified as glass and (Cr,Fe,Ni,Mn)-oxide, respectively (see Fig. 12a and Table S2). In a few small areas steel (phase III) was detected. The bottom bar shown in Fig. 12b showed a similar pattern as Fig. 12a, with the glass (phase I) and the (Cr,Fe,Ni,Mn)-oxide (phase II) covering the majority of the sample surface. However, it can be seen that the area covered by glass in the top bar was slightly smaller than the area covered by glass in the bottom bar. Additionally, in the areas where the steel signal (phase III) was detected on the top bar, the bottom bar was covered by a Cr-rich-oxide (phase IV) with a very low Mn, Fe, and Ni content. These SEM observations suggest that the fracture occurred primarily inside the glass, or inside the oxide scale. Directly next to the areas where the fracture occurred in the glass, there seems to be a small area where the fracture occurred at the glass/oxide interface, this is why the glass area is larger in the bottom bar than the top bar. Only in few places the fracture occurred at the oxide/steel interface. This indicates that the steel/oxide interface is the strongest in this case and that the measured fracture energy for these samples, 17.7 ± 1.6 J/m^2, corresponds to the average fracture energy for the glass and the oxide scale.

The SEM micrographs taken after 3,000 h of exposure reveal that the top bar was covered primarily in phase I and phase VII, which correspond to the glass phase and steel, respectively (see Fig. 12c and Table S2). Only in small areas directly next to the glass phase a mixed (Cr,Fe,Ni,Mn)-oxide (phase VI) was found. The corresponding bottom bar (see Fig. 12d) showed a similar pattern than the top bar with a large surface coverage of glass (phase I) and Cr oxide (phase VIII) and only a small surface coverage of a mixed (Cr,Fe,Ni,Mn)-oxide (phase IX). The latter phase (phase IX) was again found directly next to the areas covered with glass. Unlike for the shorter exposure length the area of the

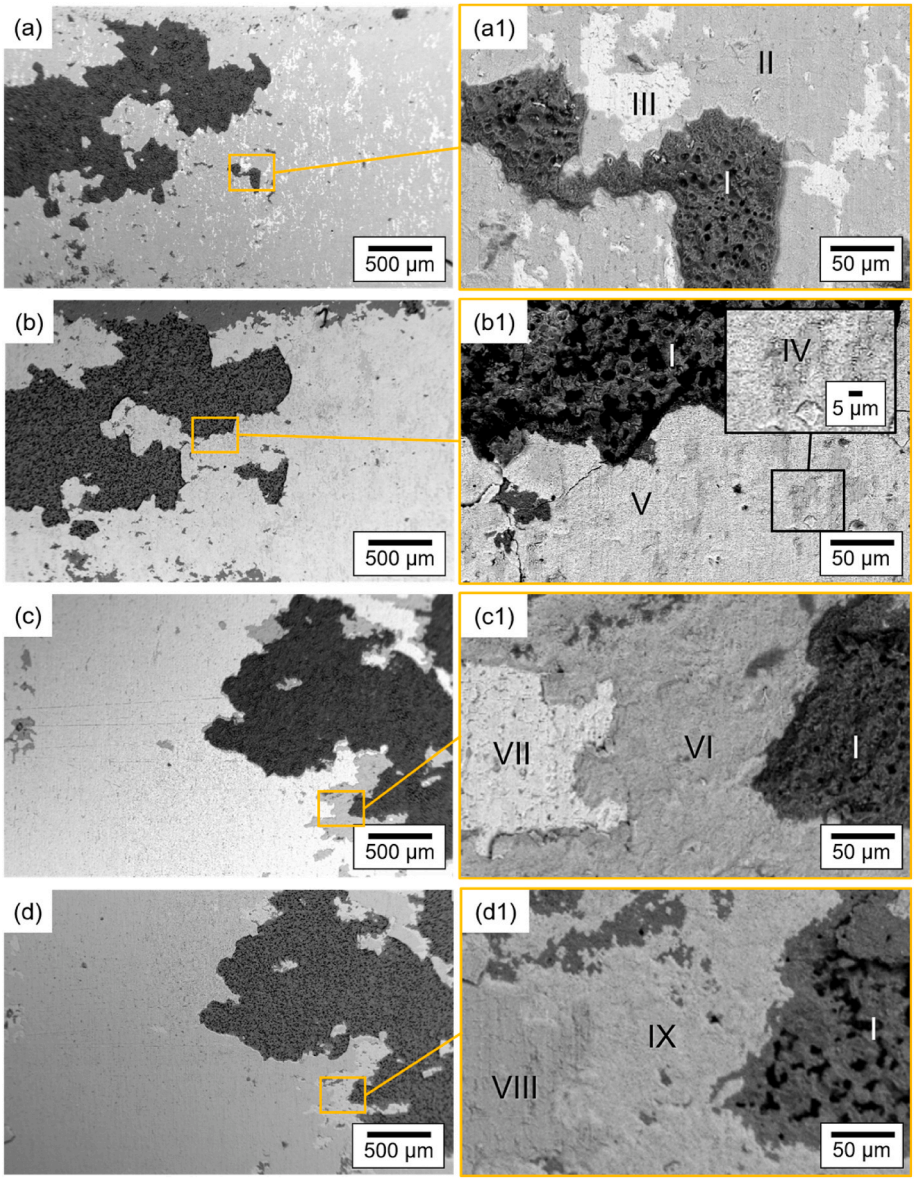

Fig. 12. SEM micrographs of the fracture interface of Ce/FeNi coated AISI 441, which was exposed at 750 °C to stagnant laboratory air for 300 h (a, b) or 3,000 h (c, d). The long top bars are shown in (a) and (c) and the short bottom bars in (b) and (d). Different phases were identified as follows using EDX: glass (I), oxide-scales (II, IV, V, VI, VIII, IX), and steel (III, VII). The exact EDX compositions can be found in Table S2.

glass phase seemed to be exactly the same size for the top and the bottom bar. This indicates that for the longer exposure length the fracture occurred primarily in the glass or along the oxide/steel interface. For this sample also the other side of the gap (see Fig. 2) was analysed using SEM and the micrographs are shown in the supplementary section (see Fig 13). In contrast to the SEM micrographs shown in Fig. 12c and d, both the top and the bottom bar in Fig. 13 are nearly exclusively covered in glass. These results indicate that the measured fracture energy of 25.3 $\pm$ 1.4 J/m^2, probably corresponds to the average fracture energy of the glass and the oxide/steel interface. Additionally, the difference between the two sides next to the gaps could indicate that the fracture energy of the glass and the oxide/steel interface are very similar and the fracture occurs sometimes in one and sometimes in the other location. This also shows that the interpretation of these results is challenging, and the measurement technique might be reaching its limit. Nevertheless, the measured high fracture energies and the trends seen for these are still reliable. The uncertainty lies primarily in the question, of where the fracture occurs and if the measured fracture energy belongs to the glass, the oxide scale, the oxide/glass interface or the oxide/steel interface. This would, however, mean that the actual fracture energy of oxide/steel interface and the oxide might be even higher than what is reported here.

Overall, the fracture analysis undertaken here shows some discrepancies, such as the aforementioned issue that the fracture pattern varies already within one sample due to the inhomogeneity of the samples. Additionally, the high fracture energy of Ce/FeNi-coated 441 that was exposed for 3,000 h at 850 °C poses the question, of how the fracture energy of the entire sample can become higher than that of the glass, as this would thus be the weakest link. One possible explanation is that diffusion of elements from the coating into the glass phase are increasing the fracture toughness of the glass. This further suggests that the chosen method to analyse the fracture energy of the Ce/FeNi-coated 441 seems to reach its limitation in the present case. Nevertheless, the present results show that the Fe/Ni coated 441 shows excellent adhesion to the

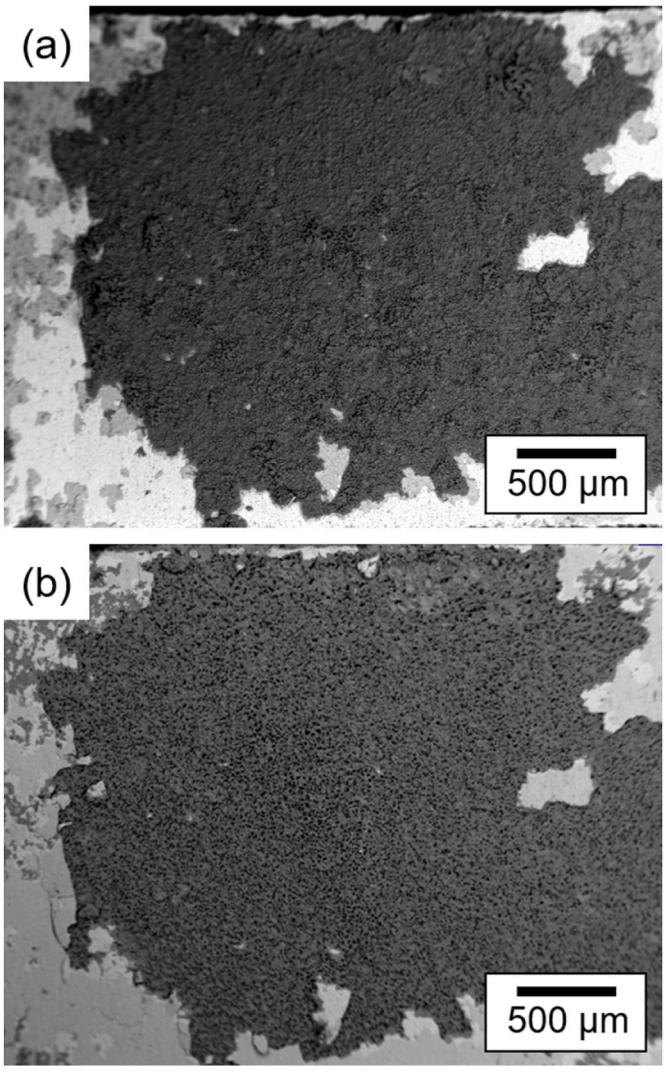

Fig. 13. Additional SEM micrographs of the fracture interface of Ce/FeNi coated AISI 441, which was exposed at 750° C to stagnant laboratory air for 3,000 h. The long top bar is shown in (a) and the short bottom bar in (b).

steel that improves even further during high temperature exposure.

4. Conclusion

To mitigate the use of Co in coatings for solid oxide cell interconnects, a Ce/FeNi coating was developed, manufactured by PVD and characterized in this work. The Cr evaporation, the ASR of the assembly, and fracture energy were measured to gauge the performance of this new coating.

Ce/FeNi- and Ce/Co-coated AISI 441 were investigated and compared to uncoated steel in both humidified (3 % H_2O) and dry air for up to 3,850 h at 850 °C. The uncoated steel showed an order of magnitude lower chromium evaporation in dry air than in humidified air. In humidified air, the Ce/FeNi-coated steel exhibited 10 times higher chromium evaporation than the Ce/Co-coated steel which is 4–5 times lower than the uncoated steel. Further exposures in dry air showed that the oxidation kinetics of Ce/FeNi-coated AISI 441 were significantly lower (50 % lower k_p) than those of Ce/Co-coated AISI 441. After the exposure, a thinner chromia scale was observed on the Ce/FeNi-coated steel.

Furthermore, the ASR was nearly 50 % lower for Ce/FeNi than for Ce/Co-coated 441 after 3,190 h of isothermal exposure at 850 °C, indicating a performance improvement. Ce/FeNi-coated steels also showed lower interfacial resistance and improved robustness against contact loss during thermal cycling. In contrast to Ce/Co-coated 441, Ce/FeNi-coated 441 also showed improved fracture toughness after 3,000 h of exposure at 750 and at 850 °C compared to 300 h of exposure.

CRediT authorship contribution statement

Mareddy Jayanth Reddy: Writing – review & editing, Writing – original draft, Visualization, Validation, Investigation, Conceptualization. **Claudia Goebel:** Writing – review & editing, Writing – original draft, Visualization, Validation, Investigation. **Anabelle Valot:** Investigation. **Ragnar Kiebach:** Writing – review & editing, Supervision, Project administration, Funding acquisition, Conceptualization. **Jan-Erik Svensson:** Funding acquisition. **Henrik Lund Frandsen:** Writing – review & editing, Supervision, Project administration, Funding acquisition, Conceptualization. **Jan Froitzheim:** Writing – review & editing, Supervision, Project administration, Funding acquisition, Conceptualization.

Declaration of competing interest

The authors declare that they have no known competing financial interests or personal relationships that could have appeared to influence the work reported in this paper.

Acknowledgements

This project has received funding from the Fuel Cells and Hydrogen 2 Joint Undertaking under Grant Agreement No 826323. This Joint Undertaking receives support from the European Union#8217; s Horizon 2020 Research and Innovation programme, Hydrogen Europe and Hydrogen Europe Research. This work was also supported by the strategic innovation program Metalliska Material (Vinnova grant 2021–01003) a joint program of VINNOVA, Formas and the Swedish Energy. This work was performed in part at the Chalmers Material Analysis Laboratory (CMAL).

Appendix A. Supplementary data

Supplementary data to this article can be found online at https://doi.org/10.1016/j.ijhydene.2025.152996.

References

[1] Choudhury A, Chandra H, Arora A. Application of solid oxide fuel cell technology for power generation - a review. Renew Sustain Energy Rev Apr. 2013;20:430–42. https://doi.org/10.1016/j.rser.2012.11.031. Pergamon.
[2] Nami H, Rizvandi OB, Chatzichristodoulou C, Hendriksen PV, Frandsen HL. Techno-economic analysis of current and emerging electrolysis technologies for green hydrogen production. Energy Convers Manag 2022;269:116162. https://doi.org/10.1016/j.enconman.2022.116162.
[3] 'Fuel cells for data centers | Bosch SOFC'. Accessed: January. 18, 2023. [Online]. Available: https://www.bosch-sofc.com/applications/data-center/.
[4] MultiPLHY - project MultiPLHY. https://multiplhy-project.eu/. [Accessed 22 January 2024].
[5] Horita T. Chromium poisoning for prolonged lifetime of electrodes in solid oxide fuel cells - review. Ceram Int Mar. 2021;47(6):7293–306. https://doi.org/10.1016/J.CERAMINT.2020.11.082.
[6] Sohal MS, O'Brien JE, Stoots CM, Sharma VI, Yildiz B, Virkar A. Degradation issues in solid oxide cells during high temperature electrolysis. J Fuel Cell Sci Technol Dec. 2011;9(1). https://doi.org/10.1115/1.4003787.
[7] Tucker MC, Kurokawa H, Jacobson CP, Jonghe LCD, Visco SJ. A fundamental study of chromium deposition on solid oxide fuel cell cathode materials. J Power Sources Sep. 2006;160(1):130–8. https://doi.org/10.1016/J.JPOWSOUR.2006.02.017.
[8] Dogdibegovic E, et al. Performance of stainless steel interconnects with (Mn,Co)3O4-Based coating for solid oxide electrolysis. Int J Hydrogen Energy Jul. 2022;47(58):24279–86. https://doi.org/10.1016/J.IJHYDENE.2022.05.206.
[9] Shen F, Ibanez SA, Tucker MC. Dynamic oxidation of (Mn,Co)3O4-Coated interconnects for solid oxide electrolysis cells. Int J Hydrogen Energy 2023;48(86):33434–41. https://doi.org/10.1016/j.ijhydene.2023.05.110.

[10] Goebel C, Fefekos AG, Svensson JE, Froitzheim J. Does the conductivity of interconnect coatings matter for solid oxide fuel cell applications? J Power Sources Apr. 2018;383:110–4. https://doi.org/10.1016/j.jpowsour.2018.02.060.

[11] Tomas M, Asokan V, Puranen J, Svensson JE, Froitzheim J. Efficiencies of cobalt- and copper-based coatings applied by different deposition processes for applications in intermediate-temperature solid oxide fuel cells. Int J Hydrogen Energy Sep. 2022;47(76):32628–40. https://doi.org/10.1016/J.IJHYDENE.2022.07.168.

[12] Zhao Q, Geng S, Chen G, Wang F. Application of sputtered NiFe2 alloy coating for SOFC interconnect steel. J Alloys Compd Nov. 2018;769:120–9. https://doi.org/10.1016/j.jallcom.2018.07.333.

[13] Hua B, Zhang W, Wu J, Pu J, Chi B, Jian L. A promising NiCo2O4 protective coating for metallic interconnects of solid oxide fuel cells. J Power Sources Nov. 2010;195(21):7375–9. https://doi.org/10.1016/J.JPOWSOUR.2010.05.031.

[14] Paknahad P, Askari M, Ghorbanzadeh M. Application of sol–gel technique to synthesis of copper–cobalt spinel on the ferritic stainless steel used for solid oxide fuel cell interconnects. J Power Sources Nov. 2014;266:79–87. https://doi.org/10.1016/J.JPOWSOUR.2014.04.122.

[15] Zanchi E, Talic B, Sabato AG, Molin S, Boccaccini AR, Smeacetto F. Electrophoretic co-deposition of Fe2O3 and Mn1,5Co1,5O4: processing and oxidation performance of Fe-doped Mn-Co coatings for solid oxide cell interconnects. J Eur Ceram Soc Oct. 2019;39(13):3768–77. https://doi.org/10.1016/j.jeurceramsoc.2019.05.024.

[16] Sabato AG, et al. Mn-Co spinel coatings on Crofer 22 APU by electrophoretic deposition: up scaling, performance in SOFC stack at 850 °C and compositional modifications. J Eur Ceram Soc Jul. 2021;41(8):4496–504. https://doi.org/10.1016/J.JEURCERAMSOC.2021.03.030.

[17] Sun Z, Wang R, Nikiforov AY, Gopalan S, Pal UB, Basu SN. CuMn1.8O4 protective coatings on metallic interconnects for prevention of Cr-poisoning in solid oxide fuel cells. J Power Sources Feb. 2018;378:125–33. https://doi.org/10.1016/J.JPOWSOUR.2017.12.031.

[18] Zanchi E, Sabato AG, Molin S, Cempura G, Boccaccini AR, Smeacetto F. Recent advances on spinel-based protective coatings for solid oxide cell metallic interconnects produced by electrophoretic deposition. Mater Lett Mar. 2021;286:129229. https://doi.org/10.1016/J.MATLET.2020.129229.

[19] Pinto R, Carmezim MJ, Montemor MF. Electrodeposition and isothermal aging of Co and Mn layers on stainless steel for interconnectors: initial stages of spinel phase formation. J Power Sources Jun. 2014;255:251–9. https://doi.org/10.1016/J.JPOWSOUR.2014.01.028.

[20] Fu QX, Sebold D, Tietz F, Buchkremer HP. Electrodeposited cobalt coating on Crofer22APU steels for interconnect applications in solid oxide fuel cells. Solid State Ionics Jun. 2011;192(1):376–82. https://doi.org/10.1016/J.SSI.2010.03.010.

[21] Lenka RK, Patro PK, Sharma J, Mahata T, Sinha PK. Evaluation of La 0.75 Sr 0.25 Cr 0.5 Mn 0.5 O 3 protective coating on ferritic stainless steel interconnect for SOFC application. Int J Hydrogen Energy Nov. 2016;41(44):20365–72. https://doi.org/10.1016/j.ijhydene.2016.08.143.

[22] Lee S-I, et al. Highly dense Mn-Co spinel coating for protection of metallic interconnect of solid oxide fuel cells. J Electrochem Soc 2014;161(14):F1389–94. https://doi.org/10.1149/2.0541414jes.

[23] Talic B, Hendriksen PV, Wiik K, Lein HL. Thermal expansion and electrical conductivity of Fe and Cu doped MnCo2O4 spinel. Solid State Ionics Nov. 2018;326:90–9. https://doi.org/10.1016/j.ssi.2018.09.018.

[24] Xie Y, Qu W, Yao B, Shaigan N, Rose L. Dense protective coatings for SOFC interconnect deposited by spray pyrolysis. ECS Trans 2010:357–62. https://doi.org/10.1149/1.3429008.

[25] Pandiyan S, Bianco M, El-Kharouf A, Tomov RI, Steinberger-Wilckens R. Evaluation of inkjet-printed spinel coatings on standard and surface nitrided ferritic stainless steels for interconnect application in solid oxide fuel cell devices. Ceram Int 2022;48(14):20456–66. https://doi.org/10.1016/j.ceramint.2022.04.003.

[26] Han GD, et al. Fabrication of lanthanum strontium cobalt ferrite (LSCF) cathodes for high performance solid oxide fuel cells using a low price commercial inkjet printer. J Power Sources Feb. 2016;306:503–9. https://doi.org/10.1016/J.JPOWSOUR.2015.12.067.

[27] Ajitdoss LC, Smeacetto F, Bindi M, Beretta D, Salvo M, Ferraris M. Mn1.5Co1.5O4 protective coating on Crofer22APU produced by thermal co-evaporation for SOFCs. Mater Lett Mar. 2013;95:82–5. https://doi.org/10.1016/J.MATLET.2012.12.079.

[28] Molin S, et al. Microstructural and electrical characterization of Mn-Co spinel protective coatings for solid oxide cell interconnects. J Eur Ceram Soc Dec. 2017;37(15):4781–91. https://doi.org/10.1016/J.JEURCERAMSOC.2017.07.011.

[29] Puranen J, et al. Influence of powder composition and manufacturing method on electrical and chromium barrier properties of atmospheric plasma sprayed spinel coatings prepared from MnCo2O4 and Mn2CoO4 + Co powders on Crofer 22 APU interconnectors. Int J Hydrogen Energy Oct. 2014;39(30):17246–57. https://doi.org/10.1016/j.ijhydene.2014.08.016.

[30] Spotorno R, Piccardo P, Perrozzi F, Valente S, Viviani M, Ansar A. Microstructural and electrical characterization of plasma sprayed Cu-Mn oxide spinels as coating on metallic interconnects for stacking solid oxide fuel cells. Fuel Cells Oct. 2015;15(5):728–34. https://doi.org/10.1002/fuce.201400189.

[31] Grünwald N, Sohn YJ, Yin X, Menzler NH, Guillon O, Vaßen R. Microstructure and phase evolution of atmospheric plasma sprayed mn-co-fe oxide protection layers for solid oxide fuel cells. J Eur Ceram Soc Feb. 2019;39(2–3):449–60.

[32] Reddy MJ, Chausson TE, Svensson JE, Froitzheim J. 11–23% Cr steels for solid oxide fuel cell interconnect applications at 800 °C – how the coating determines oxidation kinetics. Int J Hydrogen Energy Apr. 2023;48(34):12893–904. https://doi.org/10.1016/j.ijhydene.2022.11.326.

[33] Reddy MJ, Svensson J-E, Froitzheim J. Reevaluating the Cr evaporation characteristics of Ce/Co coatings for interconnect applications. ECS Trans 2021;103(1):1899–905. https://doi.org/10.1149/10301.1899ecst.

[34] Reddy MJ, et al. Experimental review of the performances of protective coatings for interconnects in solid oxide fuel cells. J Power Sources Jun. 2023;568:232831. https://doi.org/10.1016/j.jpowsour.2023.232831.

[35] Wongpromrat W, et al. Reduction of chromium volatilisation from stainless steel interconnector of solid oxide electrochemical devices by controlled preoxidation. Corros Sci May 2016;106:172–8. https://doi.org/10.1016/j.corsci.2016.02.002.

[36] Canovic S, et al. Oxidation of Co- and Ce-nanocoated FeCr steels: a microstructural investigation. Surf Coat Technol Jan. 2013;215:62–74. https://doi.org/10.1016/j.surfcoat.2012.08.096.

[37] Brylewski T, et al. Influence of Gd deposition on the oxidation behavior and electrical properties of a layered system consisting of Crofer 22 APU and MnCo2O4 spinel. Int J Hydrogen Energy Feb. 2021;46(9):6775–91. https://doi.org/10.1016/j.ijhydene.2020.11.169.

[38] B. A. Pint, 'Progress in Understanding the Reactive Element Effect Since the Whittle and Stringer Literature Review'.

[39] Chevalier S. What did we learn on the reactive element effect in chromia scale since Pfeil's patent? Mater Corros Feb. 2014;65(2):109–15. https://doi.org/10.1002/maco.201307310.

[40] Chevalier S, Valot C, Bonnet G, Colson JC, Larpin JP. The reactive element effect on thermally grown chromia scale residual stress. Mater Sci Eng A Feb. 2003;343(1–2):257–64. https://doi.org/10.1016/S0921-5093(02)00359-3.

[41] Coatings - fuelcellmaterials. https://fuelcellmaterials.com/solutions/coatings/. [Accessed 25 July 2025].

[42] Goebel C, Berger R, Bernuy-Lopez C, Westlinder J, Svensson JE, Froitzheim J. Long-term (4 year) degradation behavior of coated stainless steel 441 used for solid oxide fuel cell interconnect applications. J Power Sources 2020;449(Feb). https://doi.org/10.1016/j.jpowsour.2019.227480.

[43] Domingo JL. Cobalt in the environment and its toxicological implications. In: Reviews of environmental contamination and toxicology. New York: Springer; 1989. p. 105–32. https://doi.org/10.1007/978-1-4613-8850-0_3.

[44] Commision E. Tackling the Challenges in commodity markets and on raw materials. https://eur-lex.europa.eu/legal-content/EN/TXT/PDF/?uri=CELEX:52011DC0025&from=EN. [Accessed 25 July 2025].

[45] Leonard ME, Amendola R, Gannon PE, Shong WJ, Liu CK. High-temperature (800 °C) dual atmosphere corrosion of electroless nickel-plated ferritic stainless steel. Int J Hydrogen Energy Sep. 2014;39(28):15746–53. https://doi.org/10.1016/J.IJHYDENE.2014.07.144.

[46] Li Y, Geng S, Chen G. Electrodeposited Ni/CeO2 mulriple coating on SUS 430 steel interconnect. Int J Hydrogen Energy Jul. 2018;43(28):12811–6. https://doi.org/10.1016/J.IJHYDENE.2018.04.117.

[47] Nielsen KA, Dinesen AR, Korcakova L, Mikkelsen L, Hendriksen PV, Poulsen FW. Testing of Ni-Plated ferritic steel interconnect in SOFC stacks. Fuel Cells Apr. 2006;6(2):100–6. https://doi.org/10.1002/FUCE.200500114.

[48] Cavichiolo LS, Nørby TH, Pantleon K, Hald J. Effects of interdiffusion in nickel coated AISI 441 steel. Mater Char 2022;194:112413. https://doi.org/10.1016/j.matchar.2022.112413.

[49] Fergus J, Hui R, Li X, Wilkinson DP, Zhang J. Interconnects. In: Solid oxide fuel cells - materials properties and performance. CRC Press; 2016. p. 195–228. https://doi.org/10.1201/9781420088847-8.

[50] Devine TM. Kinetics of sensitization and de-sensitization of duplex 308 stainless steel. Acta Metall 1988;36(6):1491–501. https://doi.org/10.1016/0001-6160(88)90216-7.

[51] Essuman E, Meier GH, Żurek J, Hänsel M, Quadakkers WJ. The effect of water vapor on selective oxidation of Fe-Cr alloys. Oxid Metals 2008;69(3–4):143–62. https://doi.org/10.1007/s11085-007-9090-x.

[52] Piccardo P, Spotorno R, Geipel C. Investigation of a metallic interconnect extracted from an SOFC stack after 40,000 h of operation. Energies May 2022;15(10):3548. https://doi.org/10.3390/en15103548.

[53] Reddy MJ, Svensson JE, Froitzheim J. Evaluating candidate materials for balance of plant components in SOFC: oxidation and Cr evaporation properties. Corros Sci Jul. 2021:109671. https://doi.org/10.1016/J.CORSCI.2021.109671.

[54] Petric A, Ling H. Electrical conductivity and thermal expansion of spinels at elevated temperatures. J Am Ceram Soc May 2007;90(5):1515–20. https://doi.org/10.1111/j.1551-2916.2007.01522.x.

[55] Holt A, Kofstad P. Electrical conductivity and defect structure of Cr2O3. II. Reduced temperatures (<~1000°C). Solid State Ionics 1994;69(2):137–43. https://doi.org/10.1016/0167-2738(94)90402-2.

[56] Crawford JA, Vest RW. Electrical conductivity of single-crystal Cr2O3. J Appl Phys Aug. 1964;35(8):2413–8. https://doi.org/10.1063/1.1702871.

[57] Zhao Q, Geng S, Chen G, Wang F. Comparison of electroplating and sputtering Ni for Ni/NiFe2 dual layer coating on ferritic stainless steel interconnect. Corros Sci Nov. 2021;192:109837.

[58] Zhao Q, Geng S, Chen G, Wang F. Initial oxidation behavior of ferritic stainless steel interconnect with sputtered NiFe2 alloy coating. Oxid Metals Jan. 2020;93(3):283–99. https://doi.org/10.1007/s11085-019-09954-6.

[59] Zhao Q, Geng S, Chen G, Wang F. Effect of NiFe2 coating thickness on high temperature oxidation and electrical behavior of coated steel interconnect. J Alloys Compd Mar. 2021;858:157746. https://doi.org/10.1016/J.JALLCOM.2020.157746.

[60] Geng S, Wang Q, Wang W, Zhu S, Wang F. Sputtered Ni coating on ferritic stainless steel for solid oxide fuel cell interconnect application. Int J Hydrogen Energy Jan. 2012;37(1):916–20. https://doi.org/10.1016/J.IJHYDENE.2011.03.160.

[61] Zhao M, Geng S, Chen G, Wang F. Thermal conversion and evolution behavior of surface scale on SOFC interconnect steel with sputtered FeCoNi coating. Corros Sci 2020;168(February):108561. https://doi.org/10.1016/j.corsci.2020.108561.
[62] You PF, Zhang X, Zhang HL, Zeng CL. Oxidation behavior of NiFe2O4 spinel-coated interconnects in wet air. Oxid Metals Oct. 2018;90(3–4):499–513. https://doi.org/10.1007/s11085-018-9851-8.
[63] Froitzheim J, Ravash H, Larsson E, Johansson LG, Svensson JE. Investigation of chromium volatilization from FeCr interconnects by a denuder technique. J Electrochem Soc 2010;157(9):B1295. https://doi.org/10.1149/1.3462987.
[64] Molin S, Jasinski P, Mikkelsen L, Zhang W, Chen M, Hendriksen PV. Low temperature processed MnCo2O4 and MnCo1.8Fe0.2O4 as effective protective coatings for solid oxide fuel cell interconnects at 750 °C. J Power Sources Dec. 2016;336:408–18. https://doi.org/10.1016/j.jpowsour.2016.11.011.
[65] Ritucci I, Talic B, Kiebach R, Frandsen HL. High toughness well conducting contact layers for solid oxide cell stacks by reactive oxidative bonding. J Eur Ceram Soc 2021;41(4):2699–708. https://doi.org/10.1016/j.jeurceramsoc.2020.11.021.
[66] Ritucci I, et al. A Ba-free sealing glass with a high coefficient of thermal expansion and excellent interface stability optimized for SOFC/SOEC stack applications. Int J Appl Ceram Technol Jul. 2018;15(4):1011–22. https://doi.org/10.1111/IJAC.12853.
[67] Farzin YA, Ritucci I, Talic B, Kiebach R, Frandsen HL. Fracture toughness of reactive bonded Co–Mn and Cu–Mn contact layers after long-term aging. Ceram Int Jul. 2022;48(14):20699–711. https://doi.org/10.1016/J.CERAMINT.2022.04.050.
[68] Charalambides PG, Cao HC, Lund J, Evans AG. Development of a test method for measuring the mixed mode fracture resistance of bimaterial interfaces. Mech Mater Feb. 1990;8(4):269–83. https://doi.org/10.1016/0167-6636(90)90047-J.
[69] Hofinger I, Oechsner M, Bahr HA, Swain MV. Modified four-point bending specimen for determining the interface fracture energy for thin, brittle layers. Int J Fract 1998;92(3):213–20. https://doi.org/10.1023/A:1007530932726/METRICS.
[70] Ritucci I, et al. Improving the interface adherence at sealings in solid oxide cell stacks. J Mater Res Apr. 2019;34(7):1167–78. https://doi.org/10.1557/jmr.2018.459.
[71] Frandsen HL, Hendriksen PV, Johansen BS. A testing apparatus and a method of operating the same. IPC No. G01N3/18; G01N3/20. (Patent No. WO2014195304.). the World Intellectual Property Organization (WIPO); 2014.
[72] Natarajan P, Jegan A, Ganesh SS. Development of numerical model for predicting the characteristics of Ni–SiC nano composite coatings on AISI 1022 substrate. Mater Res Express May 2019;6(8):085048. https://doi.org/10.1088/2053-1591/AB1AC4.
[73] Aperam, 'Datasheet K41X', https://www.aperam.com/product/k41-1-4509/Date accessed 2024-June-25.
[74] Malzbender J, Steinbrech RW, Singheiser L. Determination of the interfacial fracture energies of cathodes and glass ceramic sealants in a planar solid-oxide fuel cell design. J Mater Res 2003;18(4):929–34. https://doi.org/10.1557/JMR.2003.0127.
[75] Hilpert K, Das D, Miller M, Peck DH, Weiß R. Chromium vapor species over solid oxide fuel cell interconnect materials and their potential for degradation processes. J Electrochem Soc Nov. 1996;143(11):3642. https://doi.org/10.1149/1.1837264.
[76] Ebbinghaus BB. Thermodynamics of gas phase chromium species: the chromium oxides, the chromium oxyhydroxides, and volatility calculations in waste incineration processes. Combust Flame Apr. 1993;93(1–2):119–37. https://doi.org/10.1016/0010-2180(93)90087-J.
[77] Opila EJ, et al. Theoretical and experimental investigation of the Thermochemistry of CrO 2 (OH) 2 (g). J Phys Chem A Mar. 2007;111(10):1971–80. https://doi.org/10.1021/jp0647380.
[78] Alnegren P, Sattari M, Froitzheim J, Svensson JE. Degradation of ferritic stainless steels under conditions used for solid oxide fuel cells and electrolyzers at varying oxygen pressures. Corros Sci Sep. 2016;110:200–12. https://doi.org/10.1016/j.corsci.2016.04.030.
[79] Hultquist G, Tveten B, Hörnlund E. Hydrogen in chromium: influence on the high-temperature oxidation kinetics in H2O, oxide-growth mechanisms, and scale adherence. Oxid Metals 2000;54(1):1–10. https://doi.org/10.1023/A:1004610626903. 2000 541.
[80] Hussain N, Qureshi AH, Shahid KA, Chughtai NA, Khalid FA. High-temperature oxidation behavior of HaSTELLOY C-4 in steam. Oxid Metals 2004;61(5):355–64. https://doi.org/10.1023/B:OXID.0000032328.23022.31.
[81] Saunders SRJ, Monteiro M, Rizzo F. The oxidation behaviour of metals and alloys at high temperatures in atmospheres containing water vapour: a review. Prog Mater Sci 2008;53(5):775–837. https://doi.org/10.1016/j.pmatsci.2007.11.001.
[82] Froitzheim J, Canovic S, Nikumaa M, Sachitanand R, Johansson LG, Svensson JE. Long term study of Cr evaporation and high temperature corrosion behaviour of Co coated ferritic steel for solid oxide fuel cell interconnects. J Power Sources Dec. 2012;220:217–27. https://doi.org/10.1016/j.jpowsour.2012.06.092.
[83] Falk-Windisch H, Claquesin J, Svensson JE, Froitzheim J. The effect of metallic Co-Coating thickness on ferritic stainless steels intended for use as interconnect material in intermediate temperature solid oxide fuel cells. Oxid Metals Feb. 2018;89(1–2):233–50. https://doi.org/10.1007/s11085-017-9782-9.
[84] Magdefrau NJ, Chen L, Sun EY, Yamanis J, Aindow M. Formation of spinel reaction layers in manganese cobaltite-coated Crofer22 APU for solid oxide fuel cell interconnects. J Power Sources 2013;227:318–26. https://doi.org/10.1016/j.jpowsour.2012.07.091.
[85] Talic B, Goebel C, Ritucci I, Persson H, Kiebach R, Frandsen HL. Area specific resistance of in-situ oxidized Mn-Cu and Mn-Co metal powders as contact layers for the solid oxide cell air side. J Eur Ceram Soc Mar. 2024;44(3):1678–87. https://doi.org/10.1016/J.JEURCERAMSOC.2023.10.055.